Gambaruto, A., Doorly, D., & Yamaguchi, T. (2010). Wall Shear Stress and Near-Wall Convective Transport: Comparisons with Vascular Remodelling in a Peripheral Graft Anastomosis. *Journal of Computational Physics*, *229*(14), 5339-5356. https://doi.org/10.1016/j.jcp.2010.03.029

Wall Shear Stress and Near-Wall Convective Transport: Comparisons with Vascular Remodelling in a Peripheral Graft Anastomosis.

A.M. Gambaruto[a,b,c], D.J. Doorly[b], T. Yamaguchi[c]

[a] *CEMAT, Dept Mathematics, Instituto Superior Técnico, Lisbon, Portugal*
[b] *Dept Aeronautics, Imperial College London, London, UK*
[c] *PFSL, Dept Bioengineering and Robotics, Tohoku University, Sendai, Japan*

Abstract

Fluid dynamic properties of blood flow are implicated in cardiovascular diseases. The interaction between the blood flow and the wall occurs through the direct transmission of forces, and through the dominating influence of the flow on convective transport processes. Controlled, in-vitro testing in simple geometric configurations has provided much data on the cellular-level responses of the vascular walls to flow, but a complete, mechanistic explanation of the pathogenic process is lacking. In the interim, mapping the association between local haemodynamics and the vascular response is important to improve understanding of the disease process and may be of use for prognosis. Moreover establishing the haemodynamic environment in the regions of disease provides data on flow conditions to guide investigations of cellular-level responses.

This work describes techniques to facilitate comparison between the temporal alteration in the geometry of the vascular conduit, as determined by in-vivo imaging, with local flow parameters. Procedures to reconstruct virtual models from images by means of a partition-of-unity implicit function formulation, and to align virtual models of follow-up scans to a common coordinate system, are outlined. A simple Taylor series expansion of the Lagrangian dynamics of the near-wall flow is shown to provide both a physical meaning to the directional components of the flow, as well as demonstrating the relation between near-wall convection in the wall-normal direction and spatial gradients of the wall shear stress.

A series of post-operative follow-up MRI scans of two patient cases with bypass grafts in the peripheral vasculature are presented. These are used to assess how local haemodynamic parameters relate to vascular remodelling at the location of the distal end-to-side anastomosis, i.e. where the graft rejoins the host artery. Results indicate that regions of both low wall shear stress and convective transport towards the wall tend to be more associated with regions of inward remodelling. A strong point-wise correlation was not found to exist however between local changes in wall location and either quantity.

Key words: Wall shear stress gradient, Taylor series of Lagrangian Dynamics, Near-Wall exchange, Flow field approximation from no-slip parameters, Steady state, Medical image reconstruction, Rigid body registration

1. Introduction

Computational modelling is becoming an important tool to aid the understanding of arterial physiology and pathology. Physiologically important parameters, such as the distribution of wall shear stress in a complex arterial geometry, are often nigh impossible to determine directly in-vivo, but can be deduced from a computational simulation. Moreover the effects of alterations in parameter values can be determined in isolation. Relating the computational simulation to the in-vivo situation is however a challenging task: not only in the assembly of procedures needed to transform image data into a series of numerical operations, but in first reducing the physiological state (with various attendant uncertainties) to a tractable model. Here we describe computational procedures to investigate the association between the geometric remodelling that occurs in an arterial bypass graft and parameters of the flow. The purpose is twinfold: firstly to outline the steps used in geometry definition and flow modelling, illustrating the use of Taylor expansion to derive near-wall information in a post-processing stage; secondly to relate the findings to hypotheses regarding wall shear and remodelling. There are necessarily numerous simplifications and uncertainties involved in the procedures used to model such a complex biological system, and even the task of determining the degree of uncertainty is difficult and computationally expensive. Currently whilst it is generally impractical to define probable confidence intervals for the whole solution, it is important to identify the stages used to set up the computational model, as described here, so that potential sources of error are identified, and to spur further work to fully quantify, or better, to reduce these.

The outline of the paper is as follows. A brief summary of the physiological background to the problem is first given. Section 2 then presents the patient data sets, describing the histology, medical image parameters and the morphology characterisation based on the vessel angles. The parameters for numerical simulations are detailed in Section 3. In Section 4 the near-wall convective transport is derived from a Taylor series expansion of the Lagrangian dynamics on the wall. In Section 5 the numerical simulations are discussed and the correlation of the vascular remodelling to the WSS and the near-wall convective transport normal to the wall are presented. Finally the conclusions are given in Section 6. Uncertainty in the geometry definitions are discussed briefly in the Appendix A. The construction of the virtual model from the medical images is detailed in Appendix B. The approach involves an implicit function formulation together with a partition-of-unity method. In Appendix C the registration procedure to optimally align all follow-up scans in a common coordinate system is detailed, allowing a means to quantitatively describe the vascular remodelling given by the conduit patency.

Vascular remodelling is part of complex cellular and biochemical processes with many influencing factors. Disease associated with remodelling includes atherosclerosis, aneurysms, angiogenesis in tumour growth, malformations and hydrocephalus, amongst others, where the mechanisms are greatly varied. Amongst these atherosclerosis and aneurysms are two of the most widely studied cardiovascular diseases and thought to be closely linked to the haemodynamics, more precisely to both the transport of solutes and bodies as well as exertion of mechanical forces, and are often considered as adaptive responses.

Studies on flow-mediated mechanotransduction suggest that sensed haemodynamic stresses generate signals and responses from a biochemical perspective, indicating an adaptive autoregulation to local factors [1, 2, 3, 4]. The response can be as fast as of the order of seconds while changes can take longer. The sensory mechanisms are usually attributed to the endothelial cells typically concerning changes in the flow or abnormal flow patterns, discussed commonly in terms of *wall shear stress* (WSS) and derived parameters (such as WSS spatial and temporal

gradients) as well as the pressure. It has been postulated that endothelial cells can sense temporal and spatial gradients in WSS which stimulate proliferation, permeability and migration [5, 1, 2].

In the case of atherosclerosis, studies indicate a correlation to low values of WSS with 1.0 Pa (10 dynes/cm^2) typically quoted as being the boundary below which the haemodynamic environment in an artery may locally be considered to be risk [6]. Other measures used to explain an increased risk of atherosclerosis are related to the WSS, such as the oscillatory shear index (OSI) [7] that is a measure of temporal gradient of WSS, the near-wall residence time (which can also be described as a function of OSI [8]), and spatial gradients of WSS [9] that are an index of WSS non-uniformity and disturbed flow [10]. Whereas there is considerable discussion as to which measure amongst mechanical signalling parameters best correlates with disease occurrence, it is generally accepted that low values of wall shear stress are undesirable [7, 8, 11]. Elevated WSS values have on the other hand been associated with aneurysm formation [12, 13]. Temporal and spatial gradients [14, 5] and temporal directional fluctuations [15] of WSS have also been studied in relation to aneurysm initiation, indicating these measures to be significant in the formation of disease. Vascular remodelling is thought partly as an adaptive response to alleviate undesired haemodynamic conditions, such as high WSS and spatial WSS gradients in aneurysm formation [13, 5], or low and disturbed WSS in anastomosis remodelling [10]. Consequently measures such as avoidance of high spatial gradients of WSS have been postulated as significant considerations for optimal geometry design [16].

While cardiovascular disease is related to the biology of the cells, the fluid mechanics (such as secondary flows, near-wall residence times [17, 8] and transport [18]) and the structural mechanics of the lumen (such as internal stresses, graft material and wall compliance [19, 17, 16]) are also thought to be significant parameters in determining the health.

The geometry of the conduits, the flow boundary conditions and constitutive models of blood and lumen wall (both for absobtion and deformation) all define the computed haemodynamics. However generally in reported studies it is the geometry which is implicated for high risk flows, such as vessel curvature, the presence of stenoses and bypass anastomoses conduit angles that are typically associated with disturbed and secondary flows [20, 21, 17, 22]. Contrary to this notion there has been a greater effort in quantifying effects of uncertainty in flow boundary conditions and constitutive models while uncertainty in the virtual model geometry have been largely sidelined. A brief but detailed approach of virtual model reconstruction and rigid body registration is presented in this work also, with the scope of giving transparency to how the virtual model definitions were obtained. Different approaches may lead to different models and subsequently different vascular remodelling is perceived, hence an inherent uncertainty given by *in vivo* patient specific studies.

In the above-mentioned literature the WSS and gradients of WSS are used as haemodynamic parameters to correlate with cardiovascular disesases and pathophysiologies, while generally lacking physical meaning associated with the fluid mechanics. It is the primary purpose of this work to illustrate a possibly useful means to examine haemodynamic data by studying the near-wall convective transport, in this way a physical interpretation of WSS and the spatial gradients of the WSS are given.

By performing a Taylor series expansion of the Lagrangian dynamics near the wall, for steady flow the leading terms are identified with the WSS for transport parallel to the wall, whereas the spatial gradients of WSS are linked to transport normal to the wall. Both these measures of the vessel haemodynamics will be used to asses the sensitivity of the computed flow to the post-operative vascular remodelling of two patients, as shown in Figure 1. The vascular remodelling is observed by post-operative *magnetic resonance imaging* (MRI) scans from which the intimal

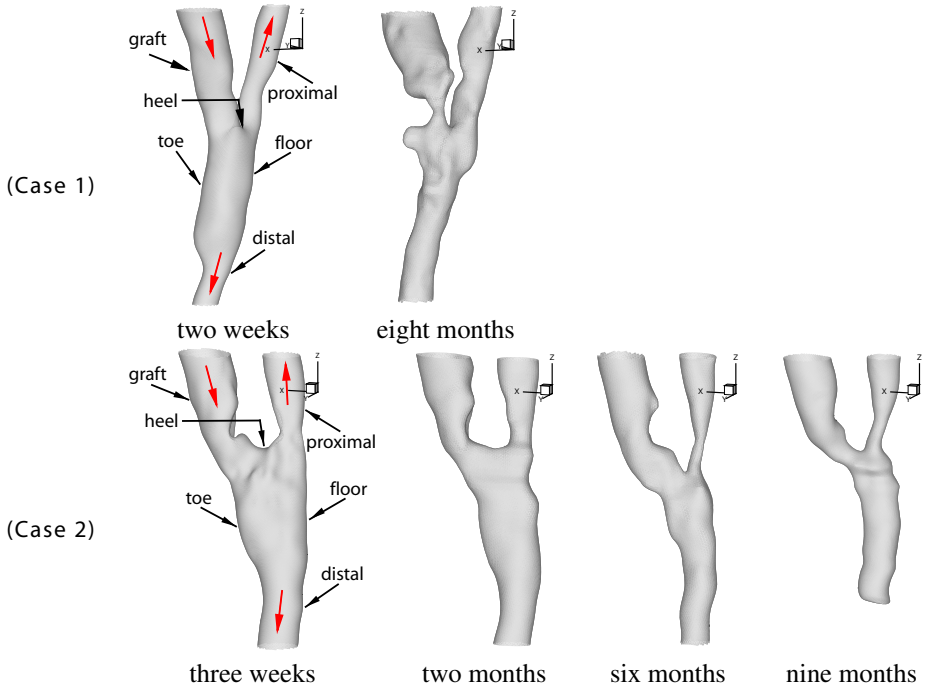

Figure 1: Distal peripheral end-to-side anastomosis geometries of two patient cases taken post-operatively. Shaded arrows indicate direction of flow. Regions termed toe, heel and floor are typical arteriosclerosis locations.

thickening is observed by lumen patency. For both patient cases, the vascular remodelling was of the form of overally loss of vessel patency over an extended period of time that brought about a second intervention, which also failed. While post-operative vascular remodelling may be affected by a series of factors, the development of atherosclerotic lesions is present in both patient cases and responsible, at least in part, for the intimal thickening and for the loss of vessel patency. Without the histology the exact nature of the wall remodelling could not be determined; some factors regarding vasculature remodelling are discussed in [23, 24, 25, 26] and references therein. It is evident however that the initial post-operative remodelling occurring in both patient cases is in accordance to those studied in [10].

2. Patient data sets

Two patient data sets are used in this work. Patient case 1 was scanned two weeks and eight months post-operatively, suffering a re-occlusion by the ninth month leading to a re-operation to insert a jump graft which also failed. Patient case 2 was scanned three weeks, two months, six months and nine months post-operatively, suffering a re-occlusion by the thirteenth month leading to a re-operation to insert a jump graft which also failed. The patient case information at time of study is as follows: case 1 - male, 74 yrs old, pathological history of partial gastrectomy and cholecystectomy, vascular risk factors of smoking, hypercholesterolaemia, hypertension;

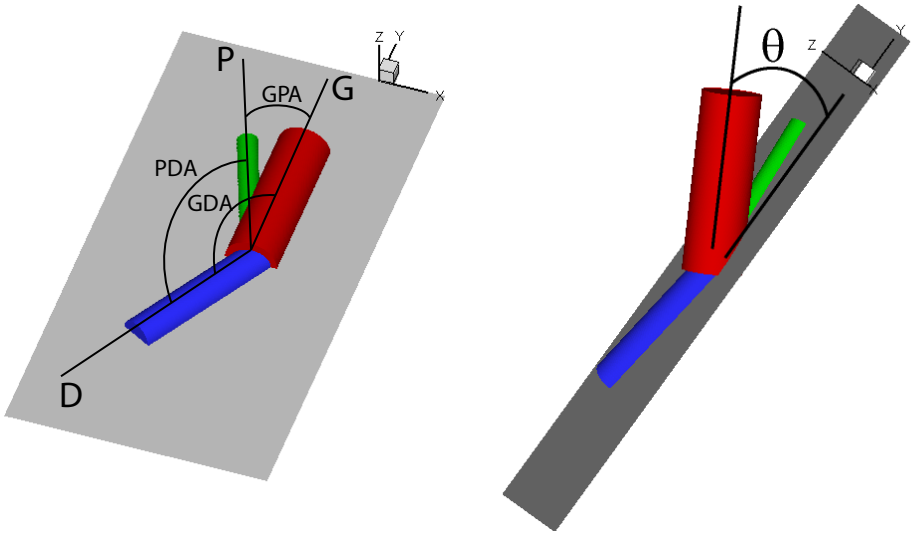

Figure 2: The characteristic angles of an anastomosis in a model case, given as the minimum angles subtended.

case 2 - male, 45 yrs old, no pathological history, vascular risk factors of smoking, diabetes and hypertension. Both subjects thus posess attributes representing significant risk of arterial disease.

Both distal peripheral end-to-side anastomosis are located in the leg, more specifically case 1 is located anterior tibial and case 2 is located below-knee popliteal, both bypasses were performed using the tunneled technique and the long saphenous vein for the graft conduit. By fitting a least squares line through the medial axis for each of the proximal, distal and bypass conduits, the geometry of the anastomosis is studied with respect to the planarity [21, 27] as shown in Figure 2. For case 1 the minimum angles subtended by these best fit lines are GPA=26^o, GDA=152^o, PDA=172^o, $\theta = 30^o$; while for case 2 GPA=26^o, GDA=150^o, PDA=173^o, $\theta = 1^o$; where GPA is the graft-proximal angle, GDA is the graft-distal angle, PDA is the proximal-distal angle and θ is the out of plane angle of the graft. For more information on the patient data sets the reader is referred to [21].

The model boundary for the simulations are obtained using *magnetic resonance imaging* (MRI) and comprising of 52 and 35 images for cases 1 and 2, respectively, in the axial plane with resolution parameters: 512×512 pixels of 0.254×0.254 mm size, 1.5 mm slice thickness and spacing. The segmentation of the medical images to define the lumen boundary is performed by using a constant value of the grey-scale for each image and is obtained initially automatically and then retouched manually. The automatic method used is that proposed in [27] which selects the grey-scale value about which there is the least change in the boundary definition. The manual retouching involved elimination of obvious noisy features captured in the segmentation procedure.

Variability in the virtual model definition, given by possible different automatic segmentation algorithms or unreproducability in user intervention, may lead to different flow solutions, as indicated clearly in [27], and different perceived progression of the vascular remodelling. To partly reduce effects of uncertainty in the geometry definition as well as in flow parameters and boundary conditions that are inevitable when using *in vivo* data, flow measures and remodelling

that can be considered to be large, hence outside the uncertainty bounds, are used in ascribing quantitative measures, as discussed later.

For consistency and given the delicate importance of variability and uncertainty, the procedures for virtual model reconstruction from the segmented images and for geometry registration that is used to align and identify regions of vessel remodelling are briefly described in the appendix, however for greater detail the reader is referred to [27, 21, 28, 29].

3. Numerical Simulation Parameters

Flow boundary conditions were obtained from *in vivo* measurements using Doppler ultrasound. For both patient cases the Reynolds number based on the bypass conduit inflow diameter and considering the mean inflow velocity was found to be Re=135, low enough for the flow to be considered laminar. The mean outflow split was found to be 40% proximal and 60% distal. Blood is assumed to be an incompressible Newtonian fluid with the kinematic viscosity of blood $\nu = 0.004/1030 = 3.9 \times 10^{-6}$ m^2 s^{-1}. The computed flow is modelled as steady, using a Poiseuille flow profile as the inflow boundary condition, this being the fully developed flow in a straigth pipe to avoid transients, and while not physiologically observed exactly it is appropriate for steady state simulation boundary conditions. The resulting mean inflow velocity for both patient cases is approximately 0.1 m s^{-1}, since the vessel diameter is 5 mm for case 1 and 4.8 mm for case 2; the corresponding wall shear stress for pipes of these calibers would be 0.67 Pa and 0.7 Pa for cases 1 and 2 respectively.

The numerical schemes are based on finite volume solutions of the steady incompressible, Newtonian, Navier-Stokes equations using Fluent V6.2.1[30]. The pressure was solved using a second-order accurate scheme, the pressure–velocity is coupled using the SIMPLE method and the momentum is approximated using a third-order upwind scheme. The segregated approach to solving the algebraic equations of continuity and momentum is used.

To perform numerical simulations, the inflow and outflow regions are extended by five radii in the vessel coaxial direction to a circular cross-section, in this way reducing the sensitivity to the boundary conditions in the region of the anastomosis. The vessel walls are taken to be rigid as the anastomosis lies in the peripheral vasculature where displacements are considered to be small [21].

Steady state was considered an acceptable condition for this study given the uncertainty and variability of physiological conditions and that peripheral arteries show a less pronounced pulsatility of the blood flow. It has been reported that the unsteady flow field at a given time is not significantly different from the steady flow field determined by the instantaneous pressure gradient [21, 31]. Steady state simulations are increasingly repersentative of unsteady simulations with low Womersley number $\alpha = R(\frac{\omega}{\nu})^{\frac{1}{2}}$, where R is an appropriate length scale, ω is the angular frequency of the oscillations, and ν is the kinematic viscosity. For both patient cases studied here $\alpha \approx 3$. Previous studies [22, 32] for realistic and idealised vascular geometries indicate that the flow structures which dominate under unsteady conditions are qualitatively similar to those present in the corresponding steady flow computation, while [33] indicates that for pulsatile flow the secondary flows are weaker and more localised. Studies in realistic geometries [34, 35, 36] also indicate that steady state results are in good agreement with time-averaged values over a cycle for WSS and spatial gradients of WSS, among other measures.

Furthermore, as shown in Section 4, the unsteady component of the near-wall convective transport normal to the wall is an order of magnitude smaller than for the steady state. For these

reasons this study will consider only steady flow simulations. The effects of flow pulsatility should however undoubtedly be incorporated for measures such as mixing which strongly rely on Lagrangian parameters.

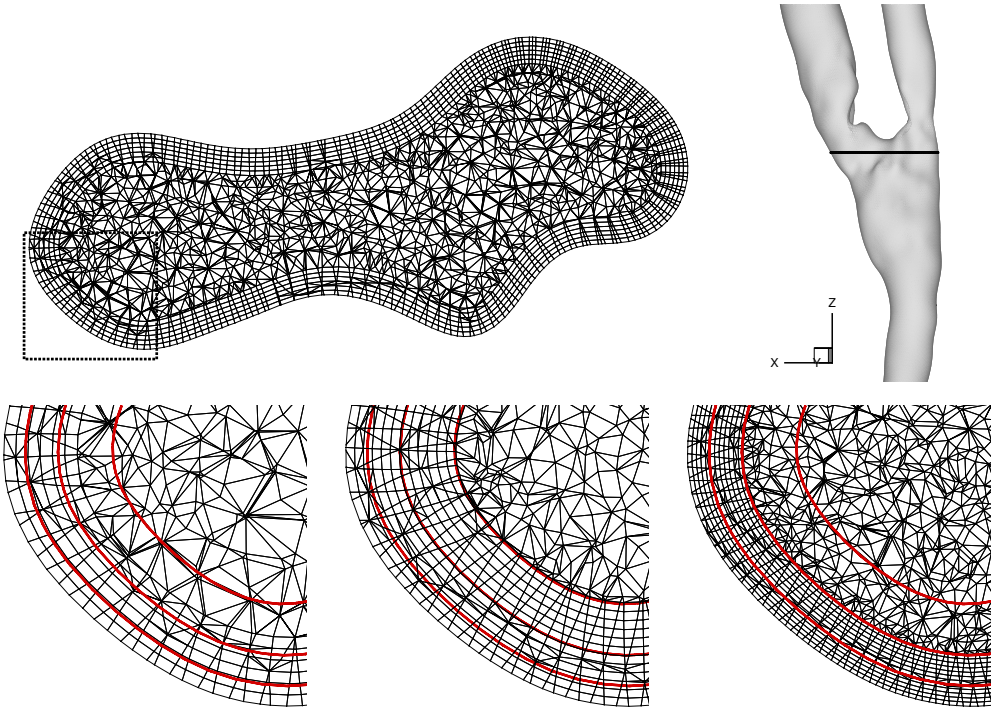

Figure 3: Cross section showing coarsest mesh resolution and slice location (same section as shown in Figure 8). Bottom row shows detail and increasing mesh resolution. The solid lines are 0.1, 0.25 and 0.5 mm projections of the surface into the domain. Computed results for selected slice shown in Figure 8.

Volume meshes with six prismatic elements across the boundary layer were generated using TGrid [37]. The height of the prismatic elements nearest to the wall correspond to approximately 2.3% of the bypass inflow radius. The unstructured meshes contain approximately 1.7 million cells. To check accuracy of the solution with respect to mesh size, finer meshes with approximately 4.3 million cells (and 12 prismatic boundary layer elements with the height of the elements nearest to the wall corresponding to approximately 1.8% of the bypass radius) and a graded 5.7 million cells with finer resolution in the anastomosis region (and 12 prismatic boundary layer elements with the height of the elements nearest to the wall corresponding to approximately 1.1% of the bypass radius) were used. The error in WSS was of the order of 1.8% on average and standrard deviarion of 4.0% between the 1.7M and 4.3M element meshes, while 0.7% on average and 3.0% standard deviation between the 4.3M and 5.7M element meshes. The largest discrepancy occurred in the region of stagnation for patient case 2 since for the finer mesh the location shifted by an order of 2 mesh elements ($\approx$ 0.17 mm) between the 1.7M and 5.7M element meshes. For the spatial gradients of WSS the error observed was on average 7% and standard deviation 14% between the 1.7M and 5.7M element meshes. Trends in the WSS and spatial gradients of WSS did not change and indicated sufficient accuracy when using the

4.3M element meshes for this study, where extreme values of the measures are used, namely *low* WSS and *large* spatial gradients of WSS are observed in correlation to *large* displacements in the vascular remodelling, hence features more noticeable than the uncertainty (or error) bounds. Qualitative evaluation of the mesh can be gauged from Figure 3.

4. Near-wall Convective Transport

Near-wall transport to and from the wall is of importance in arterial haemodynamics from the stand point of exchange processes and interactions between flow and wall. In this study of the distal peripheral end-to-side anastomosis this transport may be considered beneficial when considering oxygen and nutrients being supplied to the wall and harmful when considering excessive low density lipids (LDL) transport to the wall.

The near-wall convective transport normal to the wall describes how the flow moves from or returns to the surface gradually as depicted in Figure 4 (distinct from similar figure in [38] used to highlight flow separation). This is in contrast to the abrupt detachment of the flow from the surface that occurs when the flow separates, which has been studied to describe the local flow topology by expanding the velocity field by a Taylor series expansion [38, 39, 40, 41, 42, 43, 44].

In the case of gradual convective transport normal to the wall, a measure of the strength is given by the surface shear line convergence (or separation) [41]; where *surface shear lines* is the term used here to describe the lines that are aligned to the tangential component of the viscous traction exerted by the flow on the wall, and sometimes termed 'limiting streamlines', 'surface streamlines' or 'skin-friction lines' elsewhere in the literature. This observation was first explained by [38, 43] by considering Figure 4 as follows. Let the flow be steady and incompressible, then mass flux is constant and is given by $\dot{m} = \rho ab\bar{\mathbf{u}}$, where $\bar{\mathbf{u}}$ is the mean velocity of the cross section. Considering the cross section to be small such that the wall shear stress magnitude is given by $\tau_w = \mu\left(\frac{2\bar{\mathbf{u}}}{a}\right)$ and substituting, we obtain

$$\dot{m} = \text{constant} = \frac{a^2 b \tau_w \rho}{2\mu} \tag{1}$$

Rewriting this we find that $a \propto (b\tau_w)^{-1/2}$; hence for a constant wall shear stress magnitude, the convective transport normal to the wall is inversely proportional to the root of the distance between the surface shear lines. The coalescence or separation of the surface shear lines can therefore be an indication of flow moving from or returning to the surface.

A different approach to describe the near-wall convective transport is derived by considering a series expansion of Lagrangian dynamics of a fluid. While the measure was discussed first in [43] and then in passing in [44] for steady flow, we present here a clear derivation of the terms for both steady and unsteady flow. This is done in terms of the WSS gradient. Near wall residence times and convective transport parallel to the wall are also linked to the WSS and will be discussed here also.

Imagine a flow with velocity $\mathbf{u}(\mathbf{x}, t) = (u(\mathbf{x}, t), v(\mathbf{x}, t), w(\mathbf{x}, t))$ over a wall and let $(\underline{i}, \underline{j}, \underline{k})$ denote the unit vectors in the (x, y, z) directions respectively. Now let us consider a point on the wall with position vector $\mathbf{x}_{0w} = (0, 0, 0)$ and select a particle at time $t = t_0$ released from an initial position $\mathbf{x}_0 = (\delta x, \delta y, \delta z)$, then after a short time δt the separation of the particle from its initial position can be expressed by a Taylor series expansion in time, given by

$$\mathbf{x}(t_0 + \delta t) - \mathbf{x}(t_0) = \delta t \left(\frac{d\mathbf{x}}{dt}\right)\bigg|_{\mathbf{x}_0, t_0} + \frac{1}{2}\delta t^2 \left(\frac{d^2\mathbf{x}}{dt^2}\right)\bigg|_{\mathbf{x}_0, t_0} + O(\delta t^3) \tag{2}$$

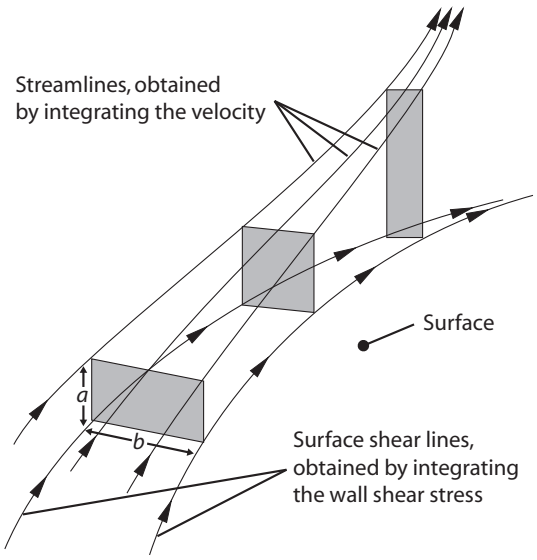

Figure 4: Surface shear lines, obtained by integrating the traction force components on the wall (here also called wall shear stress components), coalesce (or diverge) and due to continuity the fluid moves away (or towards) the wall gradually, such that $a \propto (b\tau_w)^{-1/2}$, from Equation 1, where τ_w is the wall shear stress magnitude.

where

$$\begin{aligned}\left(\frac{d\mathbf{x}}{dt}\right)\Big|_{\mathbf{x}_0,t_0} &= \mathbf{u}(\mathbf{x}_0,t_0)\\ \left(\frac{d^2\mathbf{x}}{dt^2}\right)\Big|_{\mathbf{x}_0,t_0} &= \left(\frac{d\mathbf{u}}{dt}\right)\Big|_{\mathbf{x}_0,t_0} = \left(\frac{\partial\mathbf{u}}{\partial t} + \mathbf{u}\cdot\nabla\mathbf{u}\right)\Big|_{\mathbf{x}_0,t_0}\end{aligned} \tag{3}$$

To simplify the expansion further we now consider the wall to be in the $x-z$ plane [45] such that the surface normal is the y direction. The velocity at a point near the wall $\mathbf{x}_0 = \mathbf{x}_{0w} + \delta\mathbf{x}$ can be expanded using a Taylor series expansion in space. Remembering that the velocity components at the wall are zero, the spatial gradients in the plane of the wall are zero, from continuity $\partial u/\partial x + \partial v/\partial y + \partial w/\partial z = 0$, and hence also $\partial v/\partial y = 0$, then we obtain

$$\begin{aligned}\mathbf{u}(\mathbf{x}_0,t_0) = &\left(\delta y\left(\frac{\partial u}{\partial y}\right)\Big|_{\mathbf{x}_{0w},t_0} + \frac{1}{2}\delta y^2\left(\frac{\partial^2 u}{\partial y^2}\right)\Big|_{\mathbf{x}_{0w},t_0}\right)\underline{i}\\ &+\left(\frac{1}{2}\delta y^2\left(\frac{\partial^2 v}{\partial y^2}\right)\Big|_{\mathbf{x}_{0w},t_0}\right)\underline{j}\\ &+\left(\delta y\left(\frac{\partial w}{\partial y}\right)\Big|_{\mathbf{x}_{0w},t_0} + \frac{1}{2}\delta y^2\left(\frac{\partial^2 w}{\partial y^2}\right)\Big|_{\mathbf{x}_{0w},t_0}\right)\underline{k}\end{aligned} \tag{4}$$

Making one final substitution by rewriting the velocity derivatives for a Newtonian flow in terms of the wall shear stress components

$$\frac{\tau_x}{\mu} = \left(\frac{\partial u}{\partial y}\right)\Big|_{\mathbf{x}_{0w},t_0} \quad ; \quad \frac{\tau_z}{\mu} = \left(\frac{\partial w}{\partial y}\right)\Big|_{\mathbf{x}_{0w},t_0} \tag{5}$$

we can then expand $\mathbf{x}(t_0 + \delta t) - \mathbf{x}(t_0)$ from equation 2 in its terms of the Taylor series expansion up to second order terms, distinguishing the components in the direction parallel and normal to the wall

$$
\begin{aligned}
&\mathbf{x}(t_0 + \delta t) - \mathbf{x}(t_0) = \\
&O(\delta t \cdot \delta y): && \left(\frac{\tau_x}{\mu}\right)\underline{i} + \left(\frac{\tau_z}{\mu}\right)\underline{k} \\
&O(\delta t \cdot \delta y^2): && \frac{1}{2\mu}\left(\left(\frac{\partial \tau_x}{\partial y}\right)\underline{i} + \left(\frac{\partial \tau_z}{\partial y}\right)\underline{k}\right) - \frac{1}{2\mu}\left(\frac{\partial \tau_x}{\partial x} + \frac{\partial \tau_z}{\partial z}\right)\underline{j} \\
&O(\delta t^2 \cdot \delta y): && \frac{1}{2\mu}\left(\left(\frac{\partial \tau_x}{\partial t}\right)\underline{i} + \left(\frac{\partial \tau_z}{\partial t}\right)\underline{k}\right) \\
&O(\delta t^2 \cdot \delta y^2): && \frac{1}{2\mu}\left(\tau_x\frac{\partial \tau_x}{\partial x} + \tau_z\frac{\partial \tau_x}{\partial z} + \frac{\partial^2 \tau_x}{\partial y \partial t}\right)\underline{i} \\
& && + \frac{1}{2\mu}\left(\frac{\partial^2 \tau_x}{\partial x \partial t} + \frac{\partial^2 \tau_z}{\partial z \partial t}\right)\underline{j} \\
& && + \frac{1}{2\mu}\left(\tau_x\frac{\partial \tau_z}{\partial x} + \tau_z\frac{\partial \tau_z}{\partial z} + \frac{\partial^2 \tau_z}{\partial y \partial t}\right)\underline{k}
\end{aligned}
\tag{6}
$$

From this the dominant component normal to the wall is time independent and given by

$$
(\mathbf{x}(t_0 + \delta t) - \mathbf{x}(t_0))\underline{j} = -\frac{1}{2\mu}(\delta t \cdot \delta y^2)\left(\frac{\partial \tau_x}{\partial x} + \frac{\partial \tau_z}{\partial z}\right) \tag{7}
$$

Equation 7 describes the steady state near-wall convective transport normal to the wall and is proportional to the spatial gradients of WSS in the plane of the wall. The remaining terms are parallel to the wall. Together, the directional components give an indication of the local near-wall residence times. If the flow is unsteady, additional convective transport components normal to the wall are an order of magnitude smaller and noting that typical time gradients in peripheral end-to-side anastomoses will be small, these terms may be considered to have a lesser degree of importance in the current study.

The transport has been derived here with discussion of a planar surface; the analysis also holds for curved surfaces if the equivalent local coordinate system is used. (This can be readily verified by repeating the analysis using non-Cartesian coordinate system, such as polar coordinates, to obtain two terms for the spatial gradients of WSS perpendicular to the wall normal direction even in the presence of a non-planar wall.)

In the results discussed below, the strength of the near-wall convective transport normal to the wall is identified by the quantity $TR = \partial\tau_{\zeta_1}/\partial\zeta_1 + \partial\tau_{\zeta_2}/\partial\zeta_2$; where $\tau_{\zeta_1}/\mu = \overrightarrow{n} \cdot \nabla(\mathbf{u} \cdot \overrightarrow{\zeta_1})$ and $\tau_{\zeta_2}/\mu = \overrightarrow{n} \cdot \nabla(\mathbf{u} \cdot \overrightarrow{\zeta_2})$, with $\overrightarrow{\zeta_1}$ and $\overrightarrow{\zeta_2}$ as the perpendicular unit tangent vectors and $\overrightarrow{n}$ as the unit normal vector to the individual triangular surface elements. In this way the triangular faces are considered individually to calculate the WSS gradients as a post-processing step, and

an average at the element vertices is then performed considering all adjacent elements since the spatial gradients will be discontinuous across the elements. While TR could be normalised to various parameters in order to make the units more physically meaningful, such as the viscosity or a diffusive characteristic length scale, this is not performed here to avoid further analysis which go beyond the scope of this work. Here TR is studied with respect to its sign (negative transport is towards the wall and positive is away from the wall) as well as correlations that are independent of scaling.

5. Results and Discussion

The analysis of near-wall convective transport will be used here to asses and illustrate a possibly useful means to examine haemodynamic data. Note that the discussion and analysis of the data set is limited to the region of interest: the anastomosis geometry as shown in Figures 6-7, with the remaining portion of the conduits not being considered. The leading terms in the Taylor expansion of the transport: the WSS and spatial gradients of WSS, as well as the notion of disturbed flow patters, will be correlated to the vascular remodelling for two patient cases. While these measures have been used in published works, the results are described here in terms of the fluid mechanic near-wall convective transport. From the structural mechanics, it has been noted in [19] that the spatial gradients of WSS would be expected to generate inter–cellular tension and shearing forces on the endothelial cells which line the vessel wall.

The vascular remodelling is described in terms of the closest distance (CD) between the surface boundary definitions of the first post-operative scan (two and three weeks post-operatively for case 1 and 2, respectively) and the first follow-up scan (eight and two months post-operatively for case 1 and 2, respectively); noticeable in both patient cases as loss of patency. While remodelling can be assumed to be local, as is also indicated by Figure 1, it is important to note that the CD computed between surfaces is an approximation to the vessel wall movement in the remodelling.

Due to the evident geometric differences in the two patient cases, given by the angles and planarity of the vessels as discussed in Section 2, the resulting local haemodynamics is noticeably different while there remain similarities in the general flow patterns.

By plotting the surface shear lines (SSL) as shown in Figure 5, it is possible to identify the regions of reversed flow and stagnation points. In both cases separation occurs at the toe and heel of the anastomosis, at the end of the bypass conduit, resulting in a jet-like inflow from the graft. Due to the difference in the planarity of the vessels, the impingement location of this jet is on the floor of the anastomosis for case 2 since the planarity angle $\theta = 1^o$, while for case 1 $\theta = 30^o$ and the impingement location is on the side of the anastomosis. The curvature and branching of arteries means that a non-uniform distribution of WSS is inevitable, but at any location, the degree and pattern of non-uniformity depends on both global and local features of the specific flow conduit topology.

This flow behaviour gives rise to a complex pattern of fluid properties on the wall as shown in Figure 6, with low WSS in the regions of the toe and heel, which are regions of separated flow. On observing TR we also find a complex pattern forming, with large spatial variation from negative to positive where the flow separates at the base of the bypass graft vessel and negative values in the region of the jet impingement on the anastomosis side (case 1) and floor (case 2). Regions of transport to the wall are further distinguished in general by divergence of the surface shear lines and transport from the wall as they coalesce. It is noteworthy that the complex pattern of WSS and TR occurring in localised regions is due to local surface irregularities, which may

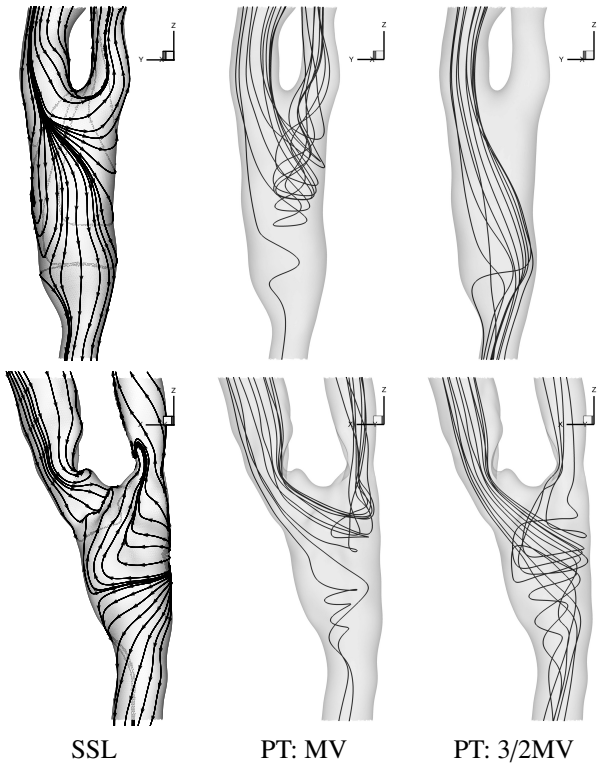

Figure 5: Flow solution for steady state condition for the two patient cases, using the first post-operative scan geometry. Results shown are surface shear lines (SSL) and particle tracks (PT). Ten particle tracks are seeded uniformly at the inflow, on either the mean velocity (PT: MV) or 3/2 mean velocity (PT: 3/2MV) rings of the Poiseuille profile inflow boundary condition.

be anatomical or given by artefacts and noise from the medical imaging [27], though these are reduced by surface smoothing as described in Appendix B. It is also worth noting that the integral of TR over the anastomosis region is close to zero ($\sim 10^{-2}$ Pa m^{-1}), as would be expected for a closed domain. The standard deviation for TR is $\sim 3\times10^{3}$ and $\sim 5\times10^{3}$ Pa m^{-1} for cases 1 and 2 respectively.

The pressure drops for both patient cases are largest where the vessels join with the anastomosis. A region of higher pressure at the location of stagnation of the jet from the bypass conduit on the anastomosis side (case 1) and floor (case 2) is also seen. The pressure drops are approximately 250 Pa and 230 Pa from the bypass inflow to the proximal and distal outflows for patient case 1, and respectively 170 Pa and 150 Pa for patient case 2. The pressure drop between the bypass root and anastomosis is approximately 30 Pa for case 1 and 80 Pa for case 2.

To visualise the free slip Lagrangian dynamics, ten uniformly spaced massless point particles are tracked from the inflow of the bypass graft, on the contour rings of both mean and 3/2 mean velocity of the imposed Poiseuille velocity profile, shown in Figure 5. It is evident that for both cases the slower moving flow tends to exit through the proximal vessel while the faster moving flow tends to exit through the distal vessel. Furthermore, it is clear that vortical structures are set

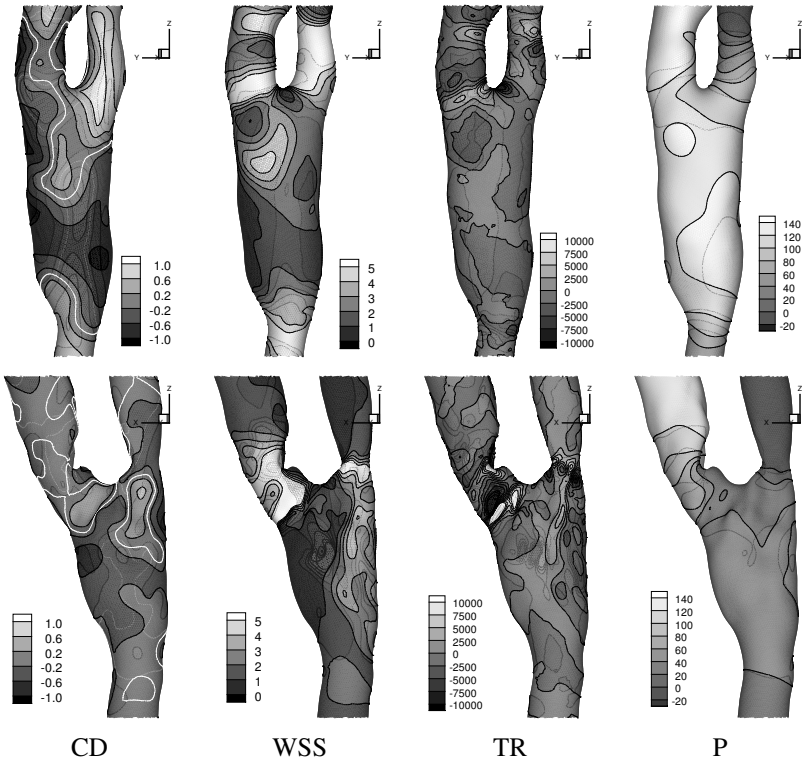

Figure 6: Flow solution for steady state condition for the two patient cases, using the first post-operative scan geometry. Results shown are wall shear stress (WSS) (/Pa), near-wall convective transport normal to the wall (TR) (/Pa m^{-1}) and relative pressure (P) (/Pa) with respect to distal outflow (P= 0 Pa). The remodelling from first post-operative scan to first follow-up scan is described by the closest distance (CD) (/mm); note that the white contour line represents CD=0 mm.

Geometry	inwards remodelling (CD<0.0 mm)		outwards remodelling (CD>0.0 mm)	
	mean WSS	mean TR	mean WSS	mean TR
Case 1	2.2	-170	4.1	130
Case 2	2.2	-280	2.3	510
	inwards remodelling (CD<-0.25 mm)		outwards remodelling (CD>0.25 mm)	
	mean WSS	mean TR	mean WSS	mean TR
Case 1	2.0	-150	4.4	390
Case 2	2.0	-250	2.8	380

Table 1: Mean values of transport normal to the wall (TR) (/Pa m^{-1}) and wall shear stress (WSS) (/Pa) for areas with negative (inwards remodelling) or positive (outwards remodelling) closest distance (CD) between first post-operative and first follow-up scan geometry surfaces. Uncertainty in geometry reconstruction is related to the pixel size (0.25 mm) and the lower portion of the table omits abs(CD)<1 pixel from analysis.

up along the floor of the anastomosis, as also discussed in [22].

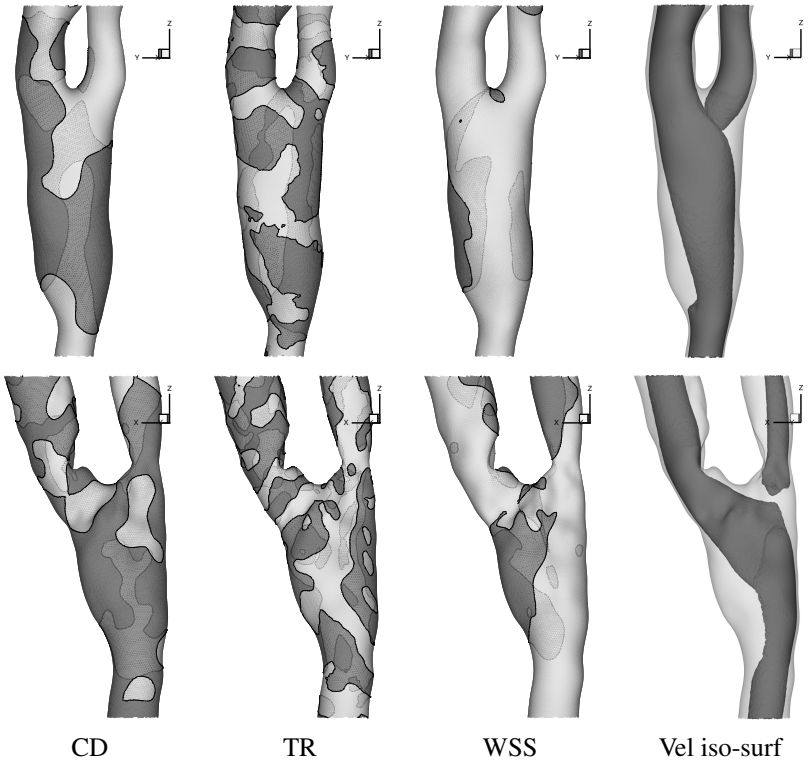

Figure 7: Qualitative correspondence of the regions of vascular remodelling given by: the closest distance (CD) between the first post-operative and first follow-up scan (black is inwards and white is outwards), the near-wall convective transport normal to the wall (TR) (black is to and white is from), the wall shear stress (WSS) (black is < 1 Pa and white is > 1 Pa), and the velocity iso-surface (Vel iso-surf) with value of 3/2 mean inflow velocity.

As shown from Figures 1 and 5 the vascular remodelling reduces the areas of recirculating fluid, with the anastomosis narrowing around the areas of faster flow as shown by the iso-surface of velocity in Figure 7. This tends to reduce the complex (or disturbed) flow patterns, and the spatial gradients of wall shear stress which yield the convective transport normal to the wall. The reduction of conduit patency occurs mostly at the toe of the anastomosis, where the WSS predicted by the steady computations is low, as well as at the the start of the graft and proximal vessel despite being regions of respectively elevated WSS and not expeceted to remodel and reduce conduit patency. On observing more closely the geometrical post-operative evolution in Figure 1, we note that the vascular remodelling tends to be inwards on the whole, as can also be seen by the closest distance map in Figure 7.

In Figure 7 the WSS and TR are shown in order to visually indicate the regions of possible correlation with the vascular remodelling, by observing the sign of TR to indicate transport to or from the wall and the magnitude of WSS for transport velocity parallel to the wall, while more detailed analysis is given in Tables 1, 2 and 3. To avoid uncertainties in medical image segmentation and the geometry registration that will inevitably occur and bias the results, the closest distances (CD) between surfaces under the pixel size (0.25 mm, approx 1/10 bypass

Geometry	inwards remodelling (CD<-0.25 mm)		outwards remodelling (CD>0.25 mm)	
	WSS<1	WSS>1	WSS<1	WSS>1
Case 1	20	42	1	37
Case 2	31	57	3	9
	TR<0	TR>0	TR<0	TR>0
Case 1	34	29	18	19
Case 2	48	40	1	11
	TR<-1000	TR>1000	TR<-1000	TR>1000
Case 1	28	13	25	34
Case 2	48	33	1	18

Table 2: Scaled percentage area of anastomosis geometry with negative (inwards remodelling) or positive (outwards remodelling) closest distance (CD) between first post-operative and first follow-up scan geometries, based on the wall shear stress (WSS) (/Pa) or the transport normal to the wall (TR) (/Pa m^{-1}). Uncertainty in geometry reconstruction is related to the pixel size (0.25 mm) and the table omits abs(CD)<1 pixel from analysis.

Geometry	CD-WSS	CD-TR	TR-WSS
	Considering all CD		
Case 1	0.45	0.08	0.01
Case 2	0.07	0.14	-0.04
	Omitting abs(CD)<0.25 mm		
Case 1	0.50	0.12	0.06
Case 2	0.16	0.35	-0.13
	Omitting abs(CD)<0.25 mm and abs(TR)<1000 Pa m^{-1}		
Case 1	0.33	0.16	0.08
Case 2	0.12	0.43	0.13

Table 3: Correlation between the closest distance (CD) (/m) moved in the vascular remodelling, the transport normal to the wall (TR) (/Pa m^{-1}) and the wall shear stress (WSS) (/Pa). Correlation of parameters omitting regions of anastomosis with abs(CD)<0.25 mm and abs(TR)<1000 Pa m^{-1} are presented in the lower portion of the table.

radius), hence abs(CD)<0.25 mm, can also be discarded from the analysis. Ignoring regions with abs(CD)<0.25 mm also signifies that only regions of noticeable vascular remodelling will be studied. Note that by ignoring CD under the pixel size in the analysis, the area of the anastomosis considered will of course be less than the whole, however in Tables 2 and 3 the percentage area is rescaled to refer to that used in the analyses to allow for direct proportional comparison.

From Table 1 we note consistently (considering all the anastomosis region or for regions of abs(CD)>0.25 mm) that the inwards vascular remodelling occurs in regions with mean WSS lower than in regions where outwards vascular remodelling occurs, though the difference is more evident for case 1 than for case 2. Furthermore, we note that the mean WSS value for regions of inwards vascular remodeling are larger than the stipulated 1 Pa that is the suggested approximate threshold for regions at risk of intimal thickening and atherogenesis. Noticeably, the regions of inwards vascular remodelling have negative mean TR (transport towards the wall) while the regions of outwards vascular remodelling have positive mean TR (transport away from the wall).

In Table 2 the distribution of WSS and TR are observed more closely for regions with

Projection distance (/mm)	case 1		case 2	
	normal	parallel	normal	parallel
0.1	0.99	0.99	0.98	0.99
0.25	0.94	0.92	0.90	0.91
0.5	0.84	0.82	0.76	0.78

Table 4: Correlation between the transport normal and parallel to the wall (TR) (/Pa m^{-1}) and the velocity components (/m s^{-1}) at a small distance along the local geometry surface normal, for the anastomosis region.

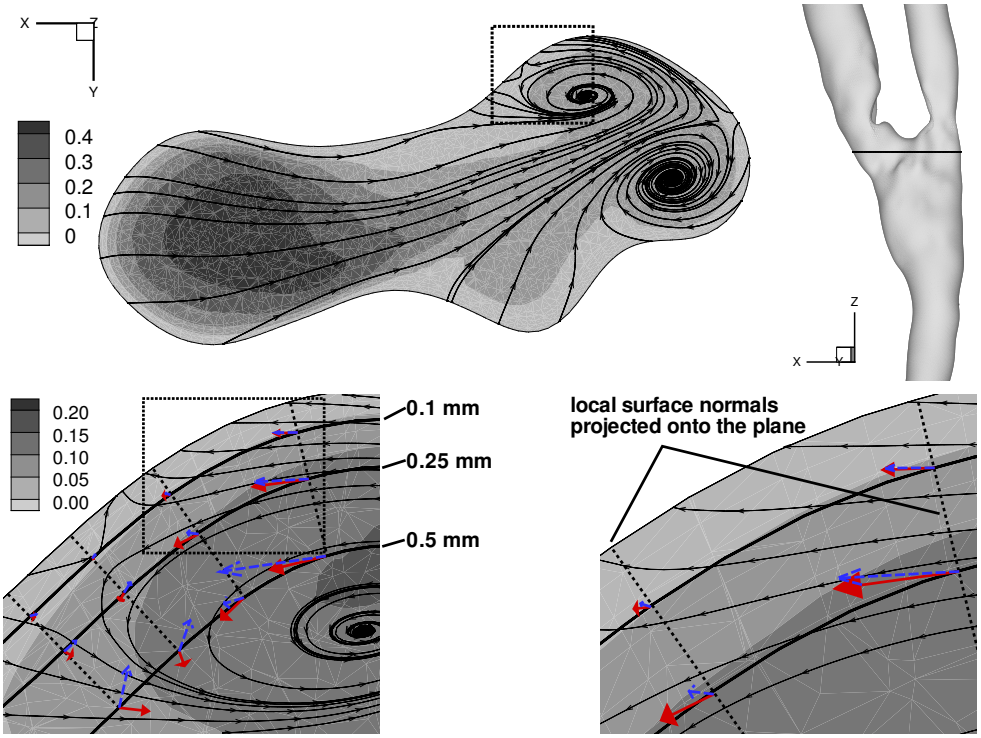

Figure 8: Top row: Cross-section and its location for patient case 2, showing velocity magnitude (/m s^{-1}) and in-plane particle paths (integration of the velocity components in the plane). Discernible features are the jet from the bypass graft on the left and on the right the impingement region on the anastomosis floor with a pair of courter-rotating vortical structures. Bottom row: details of upper right portion of cross-section at different magnification level. Concentric thick lines indicate surface outlines of anastomosis geometry projected along the local surface normal into the fluid domain at a distance of 0.1, 0.25 and 0.5 mm from the original surface definition; the dashed lines are local surface normals projected onto the plane. Arrows at cross-over locations of the projected surface outlines and projected local surface normals, indicate local in-plane velocity vectors, where solid arrows are interpolations from the computed flow field while dashed arrows are obtained by integrating the WSS and spatial gradients of the WSS.

abs(CD)>0.25 mm. Significantly the percentage area with WSS<1 Pa is greater for the inwards vascular remodelling than for the outer vascular remodelling, especially for case 1. Although the patient cases indicate a general loss of patency post-operatively, the outwards vascular remodelling has a higher ratio of area with WSS>1 Pa to area with WSS<1 Pa than is the case

for the inwards remodelling regions. These observations tend to agree with the hypothesis that WSS<1 Pa regions are more at risk to atherosclerosis, while WSS>1 Pa has an unclear influence on the possible remodelling. On observing the distribution of TR, it is apparent that the percentage area with negative TR is greater than that with positive TR for the inwards vascular remodelling regions, and vice versa for the outwards vascular remodelling regions. If only the larger values of TR are observed by ignoring regions with say abs(TR)<1000 Pa m^{-1}, which corresponds to ~10% of peak TR (see Figure 6) and is below the average abs(TR) which is ~1500 Pa m^{-1} for both cases studied, and once again scaling the percentage to only the areas analysed, we notice a greater relative association of the direction of the remodelling to the sign of TR.

In Table 3 the correlation coefficients for the various parameters observed are shown. These correlations are performed point-wise using the surface mesh definition, hence point-to-surface interpolation, and describe a stringent associativity. It is clear that for case 1 there is an evident correlation between CD (hence the vascular remodelling) and the WSS (especially if omitting regions with abs(CD)<0.25 mm), which is not true for case 2. In fact there is a greater correlation between CD and TR for case 2 (especially if omitting regions with abs(CD)<0.25 mm), which is not so for case 1. Furthermore, if only regions of higher TR are analysed by also omitting regions with abs(TR)<1000 Pa m^{-1} we note that there is an increase in the correlation between CD and TR, indicating that the regions of higher TR are more associated with the greater remodelling. For both patient cases there is apparently no correlation between the WSS and TR since they describe fluid motion parallel and normal to the wall, respectively, hence orthogonal to eachother. The degree of association between CD, TR and WSS might be stronger than indicated by the point-wise correlation performed here. The reasons for this are mainly two-fold. Firstly, due primarily to medical imaging resolution and noise, the reconstructed geometries contain small scale wall oscillations that, while reduced by surface smoothing procedures described in Appendix B, affect the local CD, TR and WSS. Secondly, the exact point correspondences between geometries is not known. In both cases, use of patches with local averages instead of point-wise correlations avoid some potential bias effects, although given the fine surface discretisation, the correlations are unlikely to be greatly affected.

As shown, the Taylor series expansion of the Lagrangian dynamics of the near-wall flow provides a physical meaning to the directional components of the flow, however it is also of interest to observe the flow behaviour at a small distance inside the fluid domain. Without performing a rigorous analysis which goes beyond the scope of this work, but is ongoing study, we look at the Lagrangian dynamics at a small distance inside the fluid domain by projecting the initial surface geometry a distance of 0.1, 0.25 and 0.5 mm (note that the bypass graft diameter $\approx$ 0.5 cm) along the local surface normal. The velocity magnitude parallel and perpendicular to the geometry surface at these distances inside the fluid domain are compared to those obtained by integrating the fluid properties at the wall, namely the wall shear stress (WSS) and the near-wall convective transport (TR). The correlation of these is detailed in Table 4 and is seen to be very strong, with a decrease as the distance from the geometry surface increases.

To indicate this visually a cross-section of the anastomosis of case 2 is shown in Figure 8, with the velocity magnitude, in-plane particle paths (obtained by integrating the velocity components in the cross-sectional plane) and the surface outlines of the projected geometries inside the fluid domain. A complex flow field is present with the jet from the bypass graft, region of impingement on the anastomosis floor and a pair on courter rotating vortical structures clearly identifiable. It is evident however that even in regions of complex geometry and associated complex flow structures, within the fluid dynamic range pertinent to the problem, there is an

appreciable near wall region within which flow can be approximately determined from the WSS and spatial gradients of WSS, as indicated also by the correlation detailed in Table 4. This yields a powerful means to probe and describe the free-slip domain from the no-slip region; furthermore it permits a greater association of the flow parameters on the wall to the core flow field.

In terms of scaling, note finally that from Equation 6, keeping the leading terms only, the ratio of velocities normal and parallel to the wall are given by $vel_{ratio} = (TR \times \delta y)/(WSS \times 2)$. Taking the example of TR=1000 Pa m^{-1}, WSS=1 Pa and $\delta y = 0.1$ mm, then $vel_{ratio} = 0.05$; whilst at $\delta y = 0.25$ mm $vel_{ratio} = 0.125$.

6. Conclusions

Computational predictions of steady flow in two patient-specific peripheral arterial bypass graft configurations were performed to derive spatial distributions of wall shear stress and to investigate the association between vascular remodelling and the local flow conditions. It was shown that all components of the near wall velocity field can be recovered by a Taylor expansion in terms of components of WSS and their gradients. For the geometries and flow regimes considered, retaining just the dominant term in the Taylor expansion to derive each velocity component correlated to better than 0.9 with the true velocity field, as far as 0.25mm from the wall, as shown in Figure 4. Since the spatial gradients of WSS determine the near-wall normal convective velocities, the purpose of the study was to investigate the degree of association between vascular remodelling, the wall shear stress and gradients in the wall shear stress components, labelled TR for transport.

From Table 1 it was found that the inwards vascular remodelling has on average a lower WSS and a preferred transport to the wall in both cases, while outwards vascular remodelling has on average a proportionally higher WSS and a preferred transport away from the wall. Correlation of these parameters, as shown in Table 3, indicates generally stronger correlations where data is limited to those above threshold values. With or without thresholding, the results show that for patient case 1 there is positive correlation of vascular remodelling to the WSS and little correlation to TR; the opposite is found for patient case 2.

The flow simulations presented are based on *in vivo* data and are subject to errors. For completeness, the techniques of virtual model reconstruction from medical images and optimal alignment of all follow-up scan geometries to a common coordinate system have been detailed in the accompanying appendix. These procedures have been used to describe the vascular remodelling in terms of change in vessel patency, given as a closest distance map between the first post-operative and the first follow-up scan geometry surface definitions. Using the data set of patient case 2, automatic image segmentation and surface smoothing are performed and a set of virtual model definitions are obtained, that are studied to gauge the uncertainty or error associated with the above findings. For these, two regions of inwards remodelling are selected: the magnitude of the WSS and TR are found to change by up to ~50% (Table 5), while trends of average values match the findings stated above for the remodelling.

While near-wall phenomena are important to understand normal or pathological cardiovascular behaviour, in the latter case such as aneurysms and atherosclerosis, the mechanisms involve complex cellular and biochemical processes. These are clearly not solely determined by measures of the near-wall convective transport as presented here, but nonetheless this appears promising as a potentially useful index as it provides an important insight into the local fluid mechanics. The near-wall convective transport is an key measure in physiological flows from the stand point of exchange processes and interactions between flow and solid boundary, and whilst

this work is aimed at the arterial system, application of the relation between wall shear stress and gradients is broader and of possible significant relevance elsewhere.

A. Uncertainty in Vessel Definition and Flow Field

The segmentation of virtual models from *in vivo* medical images carries an inherent uncertainty. Methods for image enhancement and filtering prior to the segmentation may improve contrast between the foreground objects and the background, however these can also be seen as distortions to the images that may introduce further uncertainty to the true geometry depending on the mathematical theories used. User intervention in performing segmentation procedures may help in avoiding deficits in automatic methods, however it introduces variability and non-repeatability. Uncertainty in the segmentation is further augmented by procedures in the virtual model reconstruction that involve interpolations. In computing the remodelling, variations in the rigid body registration method can yield additional uncertainty in results. Furthermore the geometric uncertainty of the model definition has a highly non-linear effect on the resulting computed flow field, that is usually of key interest in the studies. These aspects have been studied in previous work [27] and subjects of ongoing research for the authors.

Here we briefly present variations in model definition to sketch expected uncertainty bounds in the computed flow results. In Figure 9 the WSS and TR are shown for patient case 2, reconstructed with the same automatic method as discussed in Section 2, but here the entire stack is considered [27] instead of individual image slices, and also different intensities of smoothing are applied to the surface [27]. Comparison of the results in Figure 9 indicate qualitatively similar flow field however there are evident differences in WSS and TR. The two regions indicated in Figure 9, delineated by Cartesian coordinates, undergo large inwards remodelling and chosen for this reason for comparison. These regions are sensitive to the upstream flow and geometry, exhibiting complex flow structures including separation and recirculation in region (i) as well stagnation in region (ii). The average TR and WSS for these regions are detailed in Table 5. It can be seen that trends are consistent and in accordance to anastomosis averages given in Table 1. This form of uncertainty in the definition of the geometries obtained *in vivo* is important and discussed briefly, however detailed analysis of uncertainty goes beyond the scope of the work presented here.

Geometry	Region (i)		Region (ii)	
	TR	WSS	TR	WSS
G_{10}	-140	0.6	-1300	2.3
G_{100}	-110	0.4	-2300	2.3
G_U	-420	0.6	-2400	2.9

Table 5: Regional averages of WSS (/Pa) and TR (/Pa m^{-1}) in the two regions depicted in Figure 9 for the three variations of the virtual model definitions shown therein.

B. Virtual Model Reconstruction

Virtual model reconstruction is now detailed to make procedures transparent, with uncertainty in virtual model geometric definition in mind. Due to the large anisotropy in the medical image slice spacing with respect to the pixel size, a direct extraction of the desired definition is

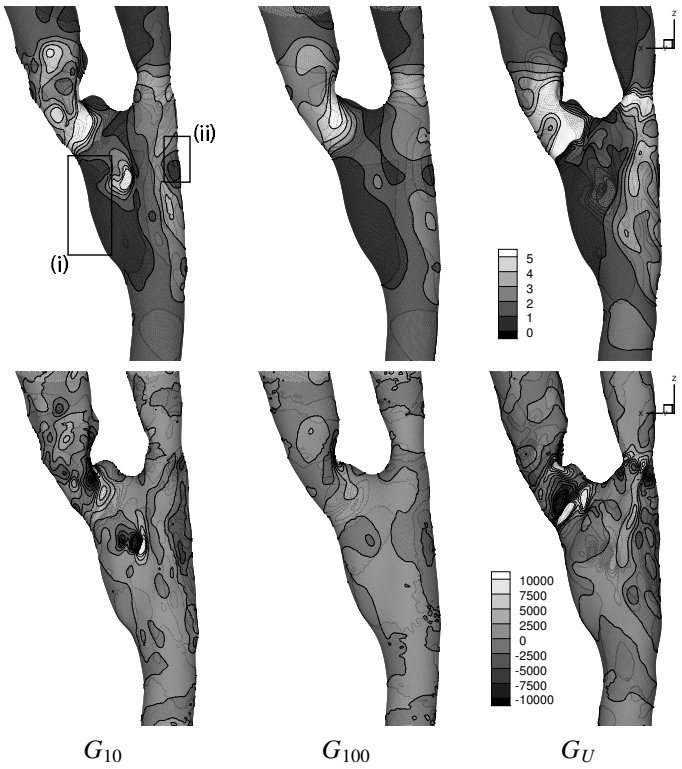

Figure 9: Flow solution for steady state condition for patient case 2 (three-week post-operative scan), with different model definitions. Geometry definition for G_{10} is obtained with constant threshold segmentation over the image stack and 10 iterations of the explicit surface smoothing scheme 'projected mean curvature flow' [27], for G_{100} the same segmentation but 100 iterations of the same smoothing scheme are used, while G_U is obtained using a user-defined segmentation and corresponds to that presented in the main section of this paper. Results shown are: top row the wall shear stress (WSS) (/Pa); bottom row the near-wall convective transport normal to the wall (TR) (/Pa m^{-1}).

not possible and an interpolation approach is required to allow for finer sampling. It should be noted that large anisotropy may lead to greater uncertainty in the virtual model definition.

The surfaces of the geometries were obtained using an implicit function formulation, with cubic radial basis function interpolation ($\phi(\mathbf{x}_i - \mathbf{x}_j) = |\mathbf{x}_i - \mathbf{x}_j|^3$, which minimises curvature variation, where $\mathbf{x}_i$ are the position vector the function is evaluated at and $\mathbf{x}_j$ are the interpolation constraints, for $\mathbf{x}_j = (x_j, y_j, z_j)$; $j = 1, \ldots, n$, where n is the number of constraints), as described in previous work [27, 46].

In brief, the surface interpolating the segmented contours is defined as the zero-level iso-surface of an implicit function $f(\mathbf{x})$. Setting $f(\mathbf{x}) = 0$ on sampled points of the cross section stack, defines the *on-surface* constraints. A gradient is formed in the implicit function by introducing further constraints at a constant close distance normal to the curve, known as *off-surface* constraints, with $f(\mathbf{x}) < -\alpha$ inside the curves and with $f(\mathbf{x}) > \alpha$ outside the curves, where α is a constant. The resulting problem is the solution of the unknown coefficients $\mathbf{c}$ from a linear system given by $f(\mathbf{x}_i) = \sum_{j=1}^{n} \mathbf{c}_j \phi(\mathbf{x}_i - \mathbf{x}_j)$, for $i = 1, \ldots, n$.

The zero-level iso-surface of the implicit function, that defines the virtual model surfaces, is

extracted using the marching tetrahedra approach [47] with linear interpolation to give an initial triangulation, that was then projected onto the true iso-surface to eliminate discretisation errors in the linear interpolation.

To reduce the computational time in the implicit function formulation as well as the marching tetrahedra method, a partition-of-unity approach [48, 49] is used, where the global domain of interest is divided into smaller overlapping subdomains where the problem can be solved locally. The local solutions are combined together by using weighting functions that act as smooth blending functions to obtain the global solution. The domain is divided into rectangular subdomain partitions, using $\mathbb{C}^1$ continuous base spline function $V(d) = 2d^3 - 3d^2 + 1$ as the weighting functions over each subdomain, where $d_i = 1 - \prod_{r \in x,y,z} \frac{4(p_r - S_r)(T_r - p_r)}{(T_r - S_r)^2}$, S_r and T_r are opposite rectangle subdomain corners, such that $0 \leq d \leq 1$ and $d = 1$ on the edges and $d = 0$ in the centre, hence $V(0) = 1, V(1) = 0, V'(0) = 0, V'(1) = 0$.

Due to the pixelated nature and the presence of noise in the medical images, the resulting virtual model surfaces are unrealistically rough and surface smoothing is necessary. Care is taken in the smoothing procedure to ensure fidelity with the medical images and the method adopted is described in greater detail in previous work [27]. The first stage of the smoothing is an explicit scheme where the severity of smoothing increases with the number of iterations performed, using the 'projected mean curvature flow' method [27, 50] which involves moving the mesh nodes using the local mesh connectivity information in order to minimise the surface roughness (curvature variation). In the second stage of the smoothing method, the surface area and volume alterations brought about in the first stage are reduced by an iterative uniform inflation of the surface along the local normal, until the distance between the smoothed and the original surface representations is minimised [27, 51].

Finally the inflow and outflow boundaries are extended to circular sections to allow implementation of Poiseuille velocity profile at inflow and reduce sensitivity of boundary conditions in the anastomosis region.

C. Geometry Registration

Registration of the reconstructed virtual models of all the post-operative follow-up scans for a patient (and sometimes inter-patient) is needed to optimally align a 3-D data set, and hence to bring the geometries to a common pose, using rigid body transformations, in order to highlight and measure differences in the morphologies and possibly the resulting flow solution. Due to the vascular remodelling the follow-up scans are not identical and correspondence between geometries is a non-trivial problem. Uncertainty in optimal pose is apparent given the difference in geometries, where sometimes common features are still perceivable but their location is distorted while other times there is no obvious correspondence. Since in this work the vascular remodelling is described by the closest distance between model surfaces, it is important to limit error in the optimal geometry alignment. Methods to optimally register geometries are discussed here with the interest in making the procedures used transparent, with uncertainty in the measurement of vascular remodelling in mind.

Given geometries G_A and G_B and the error e to be minimised, the problem is described by $e = G_A - \mathbf{R}(G_B) - \mathbf{T}$, assuming that G_A is kept fixed while G_B will undergo rigid body transforms, where $\mathbf{R}$ is the 3×3 rotation matrix, $\mathbf{T}$ is the translation vector. Note that $\mathbf{R}$ should have a determinant of 1 for no scaling to occur.

For registration, the geometries are usually considered as surfaces or volumes, but can also be described as medial lines or other decompositions [21, 27]. While any of these geometry

representations can be used, surface registration has been used primarily because the vascular remodelling is given as the closest distance between surfaces. Furthermore it has been shown in [52] for different test cases of peripheral end-to-side anastomoses, that both surface and volume registration yield similar results with the advantage that surface registration is computationally less expensive; while registration of medial lines has been found to be problematic in this work due to remodelling occurring only in local regions that alter the medial lines and yield a poor overall registration.

The registration method used in this work is an extension to that described in [28, 29] and is computationally less expensive and more elegant than equivalent methods [29, 53, 54], which have been reviewed in [55]. The registration procedure is iterative and the point correspondence is recalculated at each step. The process is known as iterative closest point (ICP), is monotonic [28] and converges to the local minimum, depending on the initial pose of the geometries. Here e is given by the average Euclidian distance between the surfaces of G_A and transformed G_B, and the minimisation is in a least squares sense, hence $\sum_{i=1}^{n} e_i^2$.

Consider a point set P_{B_i} that accurately represents G_B and the corresponding point set P_{A_i} on G_A; $i = 1, \ldots, n$, where the point correspondence of P_{A_i} is given as the closest distance locations on the surface G_A from P_{B_i}.

Let us consider a coordinate system where each point's coordinates are given with respect to the centroid of the point set it belongs to. Hence

$$P'_{A_i} = P_{A_i} - \overline{P_A} \quad ; \quad P'_{B_i} = P_{B_i} - \overline{P_B} \tag{8}$$

where

$$\overline{P_A} = \frac{1}{n}\sum_{i=1}^{n} P_{A_i} \quad ; \quad \overline{P_B} = \frac{1}{n}\sum_{i=1}^{n} P_{B_i} \tag{9}$$

The translation to minimise e in a least squares sense is given by

$$\mathbf{T} = \overline{P_A} - \mathbf{R}(\overline{P_B}) \tag{10}$$

This is to say the difference of the centroid of P_A and the centroid of the rotated P_B, however since the rotations given are about the centroids the translation is given by the difference of the centroids themselves.

Let us define the 3×3 cross-covariance matrix as

$$\mathbf{C} = \sum_{i=1}^{n} (P'_{B_i} P'^{T}_{A_i}) \tag{11}$$

and a 4×4 matrix as

$$\mathbf{N} = \begin{bmatrix} tr(\mathbf{C}) & \mathbf{K}^T \\ \mathbf{K} & \mathbf{C} + \mathbf{C}^T - tr(\mathbf{C})\mathbf{I} \end{bmatrix} \tag{12}$$

where $\mathbf{K} = \begin{bmatrix} \mathbf{C}_{23} & \mathbf{C}_{31} & \mathbf{C}_{12} \end{bmatrix}^T$ and $\mathbf{I}$ is the 3×3 identity matrix. The largest eigenvalue of $\mathbf{N}$ yields the eigenvector which is the unit quaternion $\mathbf{q} = [q_0, q_1, q_2, q_3]$ that yields the 3×3 rotation matrix which minimises e in a least-squares sense. The rotation matrix is then given by

$$\mathbf{R} = \begin{bmatrix} (q_0^2 + q_1^2 - q_2^2 - q_3^2) & 2(q_1 q_2 - q_0 q_3) & 2(q_1 q_3 + q_0 q_2) \\ 2(q_2 q_1 + q_0 q_3) & (q_0^2 - q_1^2 + q_2^2 - q_3^2) & 2(q_2 q_3 - q_0 q_1) \\ 2(q_3 q_1 - q_0 q_2) & 2(q_3 q_2 + q_0 q_1) & (q_0^2 - q_1^2 - q_2^2 + q_3^2) \end{bmatrix} \tag{13}$$

It is worthy to note that different results may be obtained if G_A is registered to G_B or vice versa. Variations and additions to this method are reviewed in [56]. The most significant involves the generation of the point correspondence and the most important addition to the basic method is the idea of outliers or inappropriate point correspondence [57, 58, 59, 60, 61] such that a point correspondence is rejected and not included in the minimisation process. Mis-registration will occur if outliers are not considered since meaningful point correspondence is otherwise enforced erroneously. For this work outliers fall into two categories: the first type is due to missing data in one of the geometries and the second type is due to geometrical difference and includes noise.

Consider the first type of outlier: missing data. In the context of this work, this is given by different length of the proximal, distal and bypass conduits being scanned for each follow up scan. This results in missing extremities of these conduits in some scans with respect to others. To solve the problem we classify the point pairs with any naked edge in the surface mesh of G_A (i.e. any edge which is part only of one mesh element) as an outlier.

The second type of outlier concerns geometrical differences, hence when two geometries are not exactly the same or some features cannot be matched exactly. Examples are morphological changes and the presence of noise. One way to identify these outliers [57, 58, 59, 60] is by placing a threshold distance for the point pairs such that any correspondence above this threshold is identified as an outlier. This threshold can be given *a priori*, as a multiple of the standard deviation [59] or, as adopted here, a percentage of the number of closest point pairs [61].

We note that while outliers have been excluded in the minimisation of the mean square distance, weighting point pairs [62, 63] can be used instead for a more gradual correspondence of points. The weighting is implemented by introducing a weighting coefficient w_i in $\mathbf{C}$

$$\mathbf{C} = \sum_{i=1}^{n} w_i (P'_{B_i} P'^{T}_{A_i}) \tag{14}$$

If $w_i = 1$ the weighing is normal while if $w_i > 1$ or $0 < w_i < 1$ the weighting is greater or less than normal, respectively, with $w = 0$ being equivalent to point pairs not being included in the minimisation of the mean square distance, hence classified as outliers. A second type of weighting involves variable point sampling of G_B such that regions of know interest may have higher sampling and hence weighting. In this work, uniform sampling of G_B was used to avoid introducing bias in this manner, which has otherwise proven to be unreliable if performed automatically.

As mentioned previously, the ICP algorithm converges to a local minimum, depending on the initial pose of G_A and G_B. A simulated re-annealing method [64] is used to generate numerous initial poses of G_B and the ICP method is run for each case, hence decreasing the possibility of missing the global minimum.

References

[1] Orr, A.W., Helmke, B.P:, Blackman, B.R., Schwartz, M.M. Mechanisms of mechanotransduction. Developmental Cell, 2006, 10:11–20.

[2] Davies, P.F. Flow-mediated endothelial mechanotransduction. Physiological Reviews, 1995, 75(3):519–560.

[3] Hahn, C., Schwartz, M.A., The role of cellular adaptation to mechanical forces in atherosclerosis. Arteriosclerosis, Thrombosis, and Vascular Biology, 2008, 28:2101-2107.

[4] Langille, B.L., O'Donnell, F., Reductions in arterial diameter produced by chronic decreases in blood flow are endothelium-dependent. Science, New Series, 1986, 231(4736):405-407.

[5] Meng, H., Wang, Z., Hoi, Y., Gao, L., Metaxa, E., Swartz, D.D., Kolega, J., Complex hemodynamics at the apex of an arterial bifurcation inducaes vascular remodeling resembling cerebral aneurysm initiation. Stroke, 2007, 38:1924-1931.
[6] Wootton, D.M., Ku, D.N., Fluid mechanics of vascular systems, diseases, and thrombosis, Annu. Rev. Biomed. Eng., 1999, 1:299–329.
[7] Ku, D.N., Giddens, D.P., Zarins, C.K., Glagov, S., Pulsatile flow and atherosclerosis in the human carotid bifurcation. Arteriosclerosis, 1985, 5(3):293–302.
[8] Himburg, H.A., Grzybowski, D.M., Hazel, A.L., LaMack, J.A., Li, Z., Friedman, M.H., Spatial comparison between wall shear stress measures and porcine arterial endothelial permeability. AJP - Heart and Circulatory Physiology, 2004, 286:1916–1922.
[9] Kleinstreuer, C., Lei, M., Archie, J.P.Jr., Flow input waveform effects on the remporal and spatial wall shear stress gradients in a femoral graft-artery connector. ASME Journal of Biomedical Engineering, 1996, 118:506-510.
[10] Ojha, M., Wall shear stress temporal gradient and anastomotic intimal hyperplasia. Circulation Research, 1994, 74:1227-1231.
[11] Gibson, C.M., Diaz, L., Kandarpa, K., Sacks, F.M., Pasternak, R.C., Sandor, T., Feldman, C., Stone, P.H., Relation of vessel wall shear stress to atherosclerosis progression in human coronary arteries. Arteriosclerosis, Thrombosis, and Vascular Biology, 1993, 13:310–315.
[12] Krex, D., Schackert, H.K., Schackert, G., Genesis of cerebral Aneurysms - An update. Acta Neurochirurgica, 2001, 143(5):429-449.
[13] Jamous, M.A., Nagahiro, S., Kitazato, K.T., Satoh, K., Satomi, J., Vascular corrosion casts mirroring early morphological changes that lead to the formation of saccular cerebral aneurysms: an experimental study in rats. Journal of Neurosurgery, 2005, 102:532-535.
[14] Shimogonya, Y., Ishikawa, T., Imai, Y., Matsuki, N., Yamaguchi, T., Can temporal fluctuation in spatial wall shear stress gradient initiate a cerebral aneurysm? A proposed novel hemodynamic index, the gradient oscillatory number (GON). Journal of Biomechanics, 2009, 42(4):550–554.
[15] Mantha, A., Karmonik, C., Benndorf, G., Strother, C., Metcalfe, R. Hemodynamics in a Cerebral Artery before and after the Formation of an Aneurysm. American Journal of Neuroradiology, 2006, 27(5):1113–1118.
[16] Lei, M., Archie, J.P., Kleinstreuer, C., Computational design of a bypass graft that minimizes wall shear stress gredients in the region of the distal anastomosis. Journal of Vascular Surgery, 1997, 25(4):637-646.
[17] Hughes, P.E., How, T.V., Flow structures at the proximal side-to-end anastomosis. Influence of geometry and flow division. ASME Journal of Biomechanical Engineering, 1995, 117:224-236.
[18] Wada, S., Karino, T. Theoretical Prediction of Low-Density Lipoproteins Concentration at the Luminal Surface of an Artery with a Multiple Bend. Annals of Biomedical Engineering, 2002, 30(6):778–791.
[19] Lei, M., Giddens, D.P., Jones, S.A., Loth, F., Bassinouny, H., Pulsatile flow in an end-to-side vascular graft model: comparison of computations with experimental data. ASME Journal of Biomechanical Engineering, 2001, 123:80-87.
[20] Staalsen, N.H., Ulrich, M., Winther, J., Pedersen, E.M., How, T., Nygaard, H., The anastomosis angle does change the flow fields at the vascular end-to-side anastomoses in vivo. Journal of Vascular Surgery, 1995, 21(3):460-471.
[21] Giordana, S., Sherwin, S.J., Peirò, J., Doorly, D.J., Crane, J.S., Lee, K.E., Cheshire, N.J., Caro, C.G., Local and global geometric influence on steady flow in distal anastomoses of peripheral bypass grafts, J. Biomech. Eng., 2005, 7(127):1087-1098.
[22] Doorly, D.J., Sherwin, S.J., Franke, P.T., Peirò, J., Vortical Flow Structure Identification and Flow Transport in Arteries. Computer Methods in Biomechanics and Biomedical Engineering, 2002, 5 (3):261–275.
[23] Gibbons, G.H., Dzau, V.J. The emerging concept of vascular remodeling. The New England Journal of Medicine, 1994, 330(20):1431-1438.
[24] Pasterkamp G., de Kleijn, D.P.V., Borst, C. Arterial remodeling in atherosclerosis, restenosis and after alteration of blood flow : potential mechanisms and clinical implications. Cardiovascular Research, 2000, 45(4):843-852.
[25] Intengan, H.D., Schiffrin E.L. Vascular remodeling in hypertension : Roles of apoptosis, inflammation, and fibrosis. Hypertension, 2001, 38(3):581-587.
[26] Glagov, S. Intimal hyperplasia, vascular modeling, and the restenosis problem. Circulation, 1994, 89(6):2888-2891.
[27] Gambaruto, A.M., Peiró, J., Doorly, D.J., Radaelli, A.G. Reconstruction of shape and its effect on flow in arterial conduits, International Journal for Numerical Methods in Fluids, 2008, 57(5):495–517.
[28] Besl, P., McKay, N., A method for registration of 3-D shapes. IEEE Transactions on Pattern Analysis and Machine Intelligence (PAMI), 1992, 14(2):239–256.
[29] Horn, B.K.P., Closed-form solution of absolute orientation using unit quaternions. Journal of Optical Society of America, 1987, 4(4):629–642.
[30] Fluent: Flow modeling software. Fluent Inc. (Lebanon, USA), *www.fluent.com*.
[31] Caro, C.G., Pedley, T.J., Schroter, R.C., Seed, W.A., The mechanics of the circulation, Oxford University Press, 1978.

[32] Lee, K.L., Doorly, D.J., Firmin, D.N., Numerical simulations of phase contrast velocity mapping of complex flows in an anatomically realistic bypass graft geometry. Medical Physics, 2006, 33(7):2621–2631.
[33] Ojha, M., Ethier, R., Johnston, K.W., Cobbold, R.S.C., Steady and pulsatile flow fields in an end-to-side arterial anastomosis model. Journal of Vascular Surgery, 1990, 12(6):747-753.
[34] Meyers, J.G., Moore, J.A., Ojha, M., Johnston, K.W., Ethier, C.R. Factors influencing blood flow patterns in the human right coronary artery. Annals of Biomedical Engineering, 2001, 29(2):109-120.
[35] Feldman, C.L., Ilegbusi, O.J., Hu, Z., Nesto, R., Waxman, S., Stone, P.H. Determination of in vivo velocity and endothelial shear stress patterns with phasic flow in human coronary arteries: a methodology to predict progression of coronary atherosclerosis. The American heart journal, 2002, 143(6):931-939.
[36] Johnston, B.M., Johnston, P.R., Corney, S., Kilpatrick, D. Non-Newtonian blood flow in human right coronary arteries: transient simulations. Journal of Biomechanics, 2006, 39(6):1116-1128.
[37] TGrid: Unstructured volume meshing. Fluent Inc. (Lebanon, USA), *www.fluent.com*.
[38] Tobak, M., Peake, D.J., Topology of three-dimensional separated flows. Ann. Rev. Fluid Mech., 1982, 14:61-85.
[39] Perry, A.E., Fairlie, B.D., Critical points in flow patterns. Adv. Geophys, 1974, 18B:299-315.
[40] Perry, A.E., Chong, M.S., A description of eddying motions and flow patterns using critical-point concepts. Ann. Rev. Fluid Mech., 1987, 19:125-155.
[41] Hornung, H.G., Perry, A.E., Some aspects of three-dimensional separation. Part I. Streamsurface bifurcations. Z. Flugwiss. Weltraumforsch., 1984, 8:77-87.
[42] Legendre, R., Séparation de l'écoulement laminaire tridimensionnel. Rech. Aéronaut., 1956, 54:3-8.
[43] Lighthill, M.J., Attachment and separation in three-dimensional flow. In Laminar Boundary Layers, ed. L. Rosenhead, pp. 72-82. Oxford: Oxford Univ. Press.
[44] Dallmann, U., Topological structures of three-dimensional flow separation. DFVLR Rep. IB 221-82-A07, Göttingen, West Ger.
[45] Franke, P.T.J., Blood flow and transport in artificial devices. Ph.D. thesis, 2002. Aeronautical Engineering, Imperial College, University of London, UK.
[46] Giordana, S., Sherwin, S.J., Peiro, J., Doorly, D.J., Papaharilaou, Y., Caro, C.G., Watkins, N., Cheshire, N., Jackson, M., Bicknall, C., Zervas, V., Automated classification of peripheral distal by-pass geometries reconstructed from medical data. Journal of Biomechanics, 2004, 38(1):47–62.
[47] Bloomenthal, J., An implicit surface polygonizer. Graphics gems IV, 2004, pp. 324–349, Academic Press Professional Inc., San Diego, CA, USA.
[48] Tobor, I., Reuter, P., Schlick, C., Efficient Reconstruction of Large Scattered Geometric Datasets using the Partition of Unity and Radial Basis Functions. Research Report RR-1301-03, Laboratoire Bordelais de Recherche en Informatique, Université Bordeaux, 2003.
[49] Pouderoux, J., Gonzato, J., Tobor, I., Guitton P., Adaptive hierarchical RBF interpolation for creating smooth digital elevation models. Proc. Geographic information systems, Washington DC, USA, November 12-13, 2004, pp. 232–240.
[50] Ohtake, Y., Belyaev, A.G., Bogaevski, I.A. Polyhedral surface smoothing with simultaneous mesh regularization. Geometric Modeling and Processing 2000 Theory and Applications, 2000, pp. 229–237.
[51] Gambaruto, A.M., Taylor, D.J., Doorly, D.J., Modelling nasal airflow using a Fourier descriptor representation of geometry. International Journal for Numerical Methods in Fluids, 2009, 59(11):1259–1283.
[52] Gambaruto, A.M. Form and Flow in Anatomical Conduits: Bypass Graft and Nasal Cavity. Ph.D thesis, 2007. Aeronautical Engineering, Imperial College, University of London, UK.
[53] Arun, K.S., Huang, T.S., Bolstein, S.D., Least-squares fitting of two 3-D point sets. IEEE Transactions on Pattern Analysis and Machine Intelligence (PAMI), 1987, 9(5):698–700.
[54] Horn, B.K.P., Hilden, H.M., Negahdaripour, S., Closed-form solution of absolute orientation using orthonormal matrices. Journal of Optical Society of America, 1988, 5(7):1127–1135.
[55] Eggert, D.W., Lorusso, A., Fisher, R.B., Estimating 3-D rigid body transformations: a comparison of four major algorithms. Machine Vision and Applications, 1997, 9(5/6):272–290.
[56] Rusinkiewicz, S., Levoy, M., Efficient variants of the ICP algorithm. Third International Conference on 3D Digital Imaging and Modeling, Quebec City, Canada, May 28 - June 1, 2001, pp.145–152.
[57] Masuda, T., Yokoya, N., A robust method for registration and segmentation of multiple range images. Computer Vision and Image Understanding, 1995, 61(3):295–307.
[58] Chetverikov, D., Svirko, D., Stepanov, D., Kersk, P., The trimmed iterative closest point algorithm. Proc. 16th International Conference on Pattern Recognition, IEEE Comp. Soc., Quebec City, Canada, August 11-15, 2002, 3:545–548.
[59] Masuda, T., Sakaue, K., Yokoya, N., Registration and integration of multiple range images for a 3-D model construction. IEEE Proc. 13th International Conference on Pattern Recognition (ICPR), Vienna, Austria, August 25-29, 1996, 1:879–883.
[60] Turk, G., Levoy, M., Zippered polygon meshes from range images. Proc. SIGGRAPH, Orlando, Florida, July

24-29, 1994, pp. 311-318.
[61] Pulli, K., Multiview registration of large data sets. Proc. 2nd Int. Conf. on 3-D Digital Imaging and Modeling, Ottawa, Canada, October, 1999, pp. 160-168.
[62] Williams, J., Bennamoun, M., A multiple view 3D registration algorithm with statistical error modelling. IEICE Transactions of Information and Systems, 2000, E83-D(8):1662–1670.
[63] Godin, G., Rioux, M., Baribeau, R., Three-dimensional registration using range and intensity information. Proceedings SPIE Videometrics III, 1994, 2350:279–290.
[64] Blais, D., Levine, M.D., Registering multiview range data to create 3D computer objects. IEEE Transactions on Pattern Analysis and Machine Intelligence (PAMI), 1995, 17(8):820–824.